

Exploring Various Techniques to Characterize Leading-Edge Dynamic Stall Onset

Sarasija Sudharsan* and Anupam Sharma[†] Iowa State University, Ames, IA 50011

We evaluate different approaches to characterize the onset of leading-edge type dynamic stall in pitching airfoils for incompressible flows. The first approach is by calculating the time variation of two flow parameters, namely, the Leading Edge Suction Parameter (LESP) and the Boundary Enstrophy Flux (BEF), both of which reach a critical value in the vicinity of stall onset. The alternate approaches include the use of Dynamic Mode Decomposition (DMD) and Wavelet Transform (WT) to identify the occurrence of critical flow states. Using wall-resolved LES results, we found that both LESP and BEF were effective in indicating stall onset, with the critical value of the BEF preceding that of the LESP. However, we were not able to identify any distinguishing behavior from DMD or WT that clearly indicates stall onset. DMD yielded unstable eigenvalues both within and outside of the stall onset regime. WT indicated the presence of energetic small scale structures, whose time of incidence varied relative to the stall onset regime for different cases with no observable trend. The novel element in the current work is the use of CFD data with fine spatial and temporal resolution within the stall onset regime, to provide a composite picture of the stall onset process using different types of analyses.

I. Introduction

The present the results of our efforts to characterize dynamic stall onset using a variety of techniques. They include dynamic mode decomposition, spectral analysis using wavelet transfer. parameter, namely, the boundary enstrophy flux (BEF), and the existing Leading Edge Suction Parameter (LESP) criterion put forth by Ramesh et al. [1]. The novel element in the current work is the focus on flow characteristics very close to stall onset, using analyses based on wall-resolved LES results. We apply three types of analyses to our datasets with fine spatial and temporal resolution to provide a composite picture of the stall onset process. We first provide an overview of the dynamic stall phenomenon, before motivating the necessity for having a stall onset criterion.

The flow over an airfoil undergoing an unsteady motion, such as pitching or plunging, remains attached upto an angle of attack α larger than the static stall angle, α_{SS} . The pitching motion increases the effective camber and causes flow to accelerate due to the Magnus effect experienced at the leading edge [2]. Further, laminar separation and reattachment near the leading edge results in the formation of a small, closed, laminar separation bubble (LSB). The transition to turbulence in the LSB increases the adverse pressure gradient that can be sustained by the airfoil without stalling. These inviscid and viscous effects induced by the unsteady motion together keep the boundary layer attached and delay flow separation. The vorticity ejected from the wall at the region of adverse pressure gradient initially remains confined to the LSB. In a classic leading-edge stall, at some α greater than α_{SS} , the bubble bursts, accompanied by a collapse in leading edge suction, due to instabilities arising from oppositely-signed vorticity that is generated, resulting in the eruption of boundary layer vorticity into the outer flow. This response of a turbulent boundary layer subjected to a persistent adverse pressure gradient is well-known [3, 4]. The ejected vorticity coalesces into a coherent dynamic stall vortex (DSV).

The DSV continues to remain attached to the leading edge but its center moves downstream as it grows, the vortex-induced lift contributing to a steeper increase in lift with increasing α . However, when the DSV is cut off from the leading edge shear layer, it convects off the airfoil surface and a severe stall (in relation to the static case) occurs. This is accompanied by large variations in aerodynamic forces and moments, that can have a detrimental effect on the wing structure. Widmann and Tropea [5] found that the DSV can be cut-off from the leading edge shear layer by either a boundary layer eruption mechanism similar to the one described above or a bluff body detachment mechanism, where a region of reverse flow grows from the trailing edge and moves upstream.

^{*}Graduate student, Aerospace Engineering, 1200 Howe Hall

[†]Associate Professor, Aerospace Engineering, 2341 Howe Hall; AIAA Associate Fellow

In attempting to characterize stall onset, it is necessary to base the criterion on observed flow features that roughly correspond to flow reaching a critical state. However, there is no standard definition of what constitutes stall onset in the literature (note, for example, the difference in the definition between [6] and [7]). In the present work, we consider the period of time when the shear layer rolls up into the DSV to indicate stall onset, since it is crucial for flow control. It has been observed that control efforts (blowing, suction etc.) are most effective in mitigating stall before this point and become less effective afterward [8]. Stall mitigation efforts might involve avoiding the formation of the DSV altogether, for example, in wind turbine blades. Or, they might involve sustaining the DSV over the airfoil for a longer period, as in fighter aircraft wings that can benefit from the vortex-induced lift[3]. In either case, characterizing stall onset is important for controlling the dynamics of the DSV. A wide range of parameters namely, the Reynolds number, pitch rate, Mach number, airfoil geometry etc. influence the type of stall and its onset. In the present work, we only consider incompressible flows and neglect Mach number effects.

As flow dynamics near the leading edge play an important part in determining stall onset, Ramesh et al. [1] proposed the use of the LESP criterion for the initiation of DSV formation, based on the leading edge limiting the maximum amount of suction to a critical value that can be supported by the airfoil. Although Narsipur et al. [9] found that at lower Reynolds numbers, the LESP continues to increase even after onset of instabilities in the LSB, nevertheless, it reaches its critical value in the vicinity of stall onset. We[10] have previously proposed a novel vorticity-based criterion, namely, the *BEF*, which reaches its critical value earlier than the *LESP*.

Aside from studying flow parameters reaching a critical value around stall onset, yet another way to describe flow reaching a critical state is to decompose the field into spatio-temporal modes growing at different rates. In most prior work, the entire flow field is considered with relatively low sampling rates in time, so that the dynamics close to the laminar separation bubble are either not resolved or are overwhelmed by the dynamics of the DSV. Mulleners and Raffel [7] applied Proper Orthogonal Decomposition (POD) to a sinusoidally pitching airfoil and observed a maximum attained by the temporal coefficient corresponding to the DSV growth mode when the DSV detaches from the leading edge. (This correlates with their definition of stall onset.) Mariappan et al. [11] studied the effect of excluding the near-wall region in DMD for dynamic stall cases and did not find a significant change in DMD modes. However, they used the entire pitching cycle for their calculations and were not focused on resolving localized instabilities around stall onset. A Lagrangian approach using Finite Time Lyanpunov Exponent (FTLE) fields[12] has also been used to study dynamic stall. Once again, this technique is applied to a large area encompassing the DSV[13] and not confined to the vicinity of the laminar separation bubble. In contrast to previous work in the literature, we use very fine resolution of boundary layer flow and frequent solution sampling in time to calculate critical flow parameters, perform modal decomposition, and map out the sequence of events occurring within the stall onset regime.

II. Methods/Details

Our analysis is based on wall-resolved large eddy simulations carried out using the compressible flow solver FDL3DI. Details on the solver can be found in [14] and details of the computational setup and grids used can be obtained from [15]. We simulated airfoils undergoing a pitch-up motion at a rate of 0.05 rad/s pivoted about the quarter-chord point, at chord-based Reynolds numbers, Re_c , of 200,000 and 500,000. The freestream Mach number, Ma, was uniformly 0.1 for all cases. In the span-wise direction, we applied periodic boundary conditions at the ends of the simulated ten percent of airfoil chord. A non-dimensional step size of 2×10^{-5} was used to advance the solution in time. All of our analyses are based on span-averaged 2D flow fields. We sampled data every 100 timesteps around the time of stall onset, leading to very fine resolution of flow during this critical period.

We carry out the three types of analyses listed in Table 1. The two evaluated flow parameters LESP and BEF are found using line integrals around the airfoil surface at each time. DMD is applied to a sequence of 2D spatial fields over a moving time window to decompose flow into modes growing at fixed frequencies. WT is used to perform non-stationary spectral analysis on a time-varying signal (pressure coefficient, C_P) at a fixed point on the airfoil.

III. Results & Discussion

We begin by defining the stall onset regime, before attempting to characterize it. The lower bound is defined following [1] and [9], as the time when a positive spike is first observed within the negative C_f distribution in the LSB, since this indicates the beginning of instabilities within the LSB. We set the upper bound for the stall onset regime as the time when DSV formation is observed from streamlines and C_p distributions over the airfoil, since control effectiveness decreases beyond this point. Thus, the stall onset regime includes the time of onset of instabilities within the LSB and

Table 1 Types of analyses used in resolving the stall onset regime

	Method	Data used	Description
1	Flow parameters - LESP and BEF	1D spatial line	Leading Edge Suction Parameter and Boundary Enstrophy Flux; line integral around airfoil at each time
2	Dynamic Mode Decomposition	2D spatial field	Sequence of spatial fields over a time window decomposed into modes; repeated with time-shifting
3	Wavelet Transform	Point on airfoil	Non-stationary spectral analysis performed on time- varying point quantity on airfoil

extends to the time of DSV formation. We next show the combined results from all of the analyses carried out (listed in section II), before providing details for each one.

A. Resolving the stall onset regime

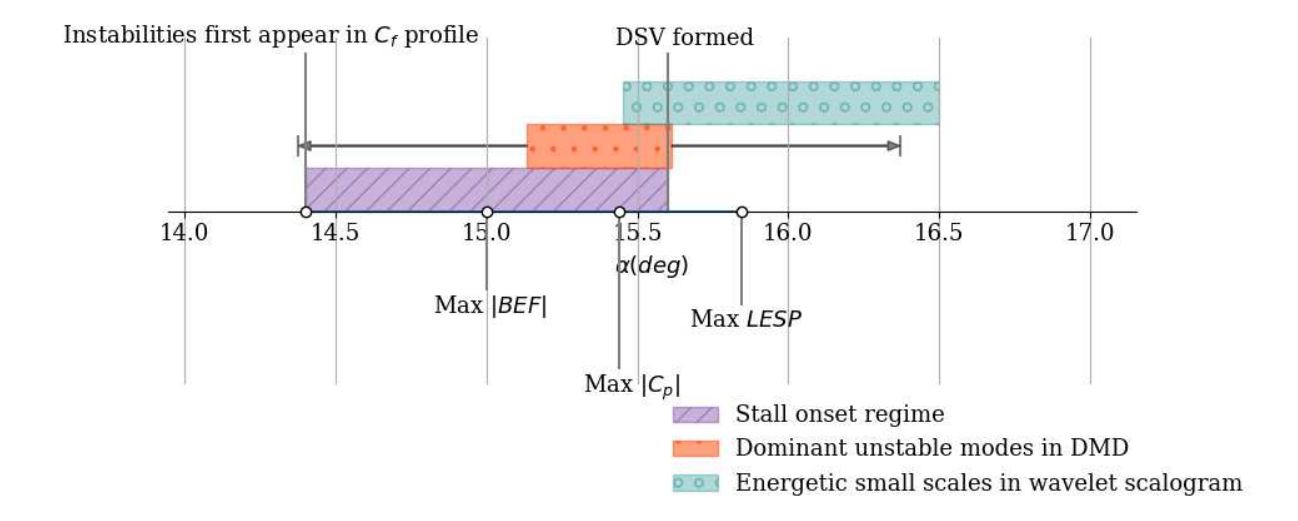


Fig. 1 Sequence of events within the stall onset regime for the SD7003 airfoil at Re_c 200,000.

Fig. 1 shows a timeline of all events for the SD7003 airfoil at Re_c 200,000. The abscissa is the angle of attack, α , which extends over the region around stall onset. The stall onset regime is shown in purple, extending between the time of onset of instabilities in the LSB and formation of the DSV. The BEF magnitude reaches a maximum first, followed by the C_p magnitude, which is shown for an indication of when leading edge suction drops. Next, the LESP reaches a maximum, though slightly outside of the stall onset regime. The orange shaded area indicates the region when modes having unstable eigenvalues from the DMD analysis also become the most dominant. It should be noted that unstable eigenvalues are observed over nearly the entire region of investigation of which only those that also corresponded to a dominant mode are highlighted. The orange area could slide either way about 0.75° (shown with arrows) since the result at each α is obtained by carrying out DMD analysis over a time window that extends on either side of it. The green shaded area indicates the region where energetic small scales are observed in the wavelet scalogram. WT is carried out using a point quantity in space (C_p at 0.1c on the airfoil suction surface), which would capture instabilities in the vicinity of the LSB. The energetic small scales are observed just before the end of the stall onset regime and lie mostly outside of it.

Fig. 2 shows the same timeline for the SD7003 airfoil at Re_c 500,000. At this higher Re_c , the stall onset regime extends over a narrower region. The maximum values of |BEF|, $|C_p|$ and LESP all lie within the stall onset regime, with the trend of $\max(|BEF|)$ preceding $\max(LESP)$ being maintained. In this case, $\max(LESP)$ lies within the stall onset region as well. The region showing unstable DMD eigenvalues belonging to dominant modes is also narrow, but is hard to pinpoint to a given time, as before. The appearance of energetic scales in the WT scalogram lies entirely

outside the stall onset regime.

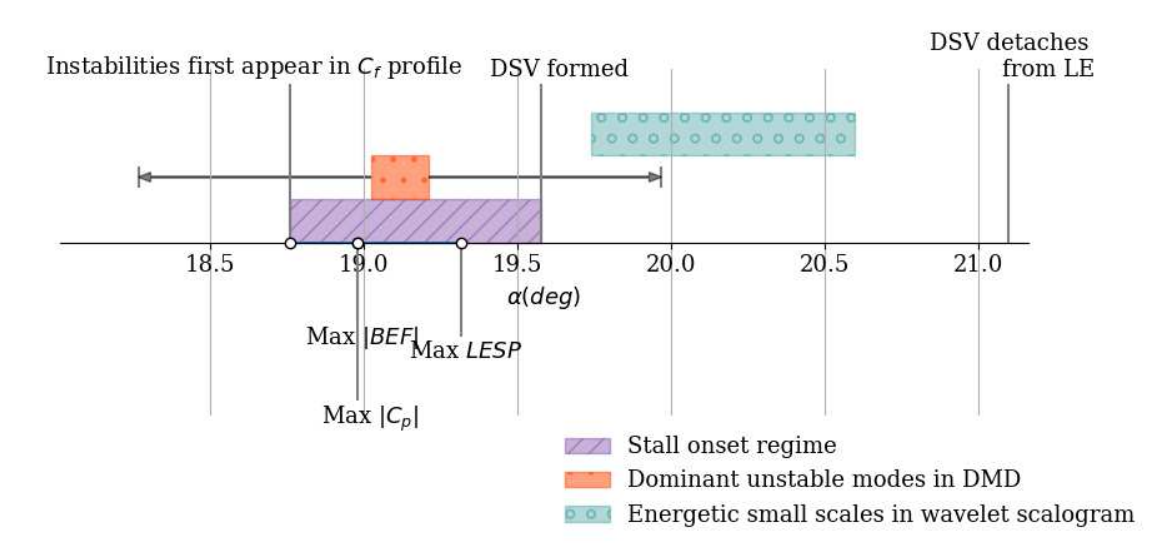


Fig. 2 Sequence of events within the stall onset regime for SD7003 airfoil at Re_c 500,000.

For the NACA0012 airfoil at Re_c 500,000, shown in 3, the stall onset regime is wider than the SD7003 airfoil at the same Re_c , indicative of a more gradual stall. The regions corresponding to DMD and WT are also wider. The flow parameters BEF and LESP display the same trend as before.

In summary, both flow parameters reach critical values mostly within the stall onset regime, with the |BEF| doing so earlier compared to the LESP. This method is also an unambiguous way to identify onset since the parameters reach a local maximum around stall onset. Use of DMD to find the unstable region is problematic in that almost the entire stall onset region is comprised of unstable modes. Also, unstable modes that are also dominant, as highlighted here, are hard to localize, since data from a sequence of time steps is used to get the eigenvalues at a given time. The small scales obtained from WT show no consistent trends on where they lie relative to the stall onset regime and are also highly dependent on the signal chosen for analysis (C_P at $0.1\,c$ on the suction surface is used here). Thus, we are unable to identify clear and consistent trends from DMD and WT analyses. Interestingly, these methods which use flow information from several time steps are less successful at indicating stall onset than the method that only depends on the flow field at a given time.

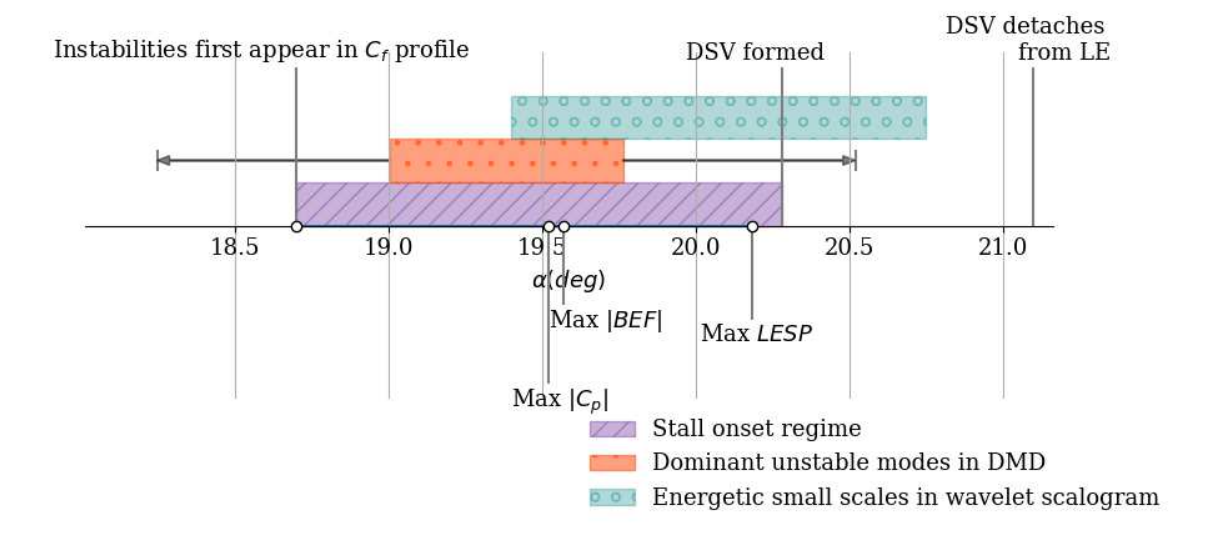


Fig. 3 Sequence of events within the stall onset regime for the NACA0012 airfoil at Re_c 500,000.

B. Critical flow parameters: LESP and BEF

We analyzed two quantities that attain a critical value around stall onset, calculated from our span-averaged LES results. One of them is the Leading Edge Suction Parameter(LESP), proposed as a criterion for the initiation of leading edge vortex formation by Ramesh et al. [1]. The other is a vorticity-based parameter, namely, the Boundary Enstrophy Flux(BEF), which represents the strengthening/weakening of wall vorticity by the vorticity flux. We have previously analyzed and compared both criteria in detail [10] and therefore present a brief overview here.

The LESP is a measure of the chord-wise suction force (F_s) at the airfoil leading edge. Its definition is given by Eq. (1), with $\hat{\bf n}$ being the unit vector normal to the airfoil surface, and $\hat{\bf e}_{\bf x}$, the unit vector in the chord-wise direction.

$$LESP = \sqrt{\frac{|F_s|}{2\pi c}}, \quad \text{where} \quad F_s = \int_{(x/c)_p}^{(x/c)_s} C_p \hat{\mathbf{n}} \cdot \hat{\mathbf{e}}_{\mathbf{x}} \, \mathrm{d}s, \tag{1}$$

The integral is carried out over the airfoil surface around the leading edge, from x/c on the pressure side to x/c on the suction side. (We have used x/c 0.25.) The criterion is based on the argument that the leading edge limits the maximum amount of suction to a critical value that can be supported by the airfoil [1]; this is achieved by vortex shedding at the leading edge.

We also look at the Boundary Enstrophy Flux (BEF) as an alternative to the LESP. Enstrophy is the square of the vorticity magnitude $|\omega|^2$. The BEF can be viewed as the integral of the product of vorticity and vorticity flux at the wall. Since we are considering 2D flow fields, only the spanwise vorticity, ω is involved in its definition, given by Eq. (2). A positive boundary enstrophy flux represents a strengthening of wall vorticity by the vorticity flux, while a negative sign represents its annihilation, each quantified by its magnitude [16].

$$BEF = \frac{1}{Re} \int_{(x/c)_p}^{(x/c)_s} \omega \frac{\partial \omega}{\partial n} ds$$
 (2)

We have previously [10] related the *LESP* to tracking the rotation of the force vector away from the chord-wise direction as the DSV coalesces, and the *BEF* to the accumulation of wall shear. Both of these criteria reach their critical values in the vicinity of stall onset, serving as clear identifiers for stall onset.

C. Dynamic Mode Decomposition

A common approach to identify a critical state occurring in flow is the use of modal decomposition. DMD[17] is used to decompose the flow field into a linear combination of spatial modes, each evolving at a fixed frequency. DMD eigenmodes are temporally orthogonal, so perturbations growing at different frequencies can be separated, as opposed to Proper Orthogonal Decomposition(POD) where the modes are spatially orthogonal. The most dominant DMD modes are determined by ranking their amplitude norms, and used to reconstruct flow evolution with time. The DMD algorithm finds the best fit linear approximation for a sequence of flow states separated in time, or 'snapshots'. The solution at any time instant $\mathbf{x}(t_k = k\Delta t)$ is written as a linear combination of the columns of Φ , the DMD modes, as shown in Eq. 3.

$$\mathbf{x}(t_k) = \sum_{\substack{i=1,r\\r < m-1}} \Phi_i \exp(\omega_i t_k) \mathbf{b_i}$$
(3)

where **b** is a vector of weights multiplying the DMD modes, found from initial conditions. Each DMD mode evolves at a specific frequency ω_i given by Eq. (4), where λ_i is the i^{th} discrete-time eigenvalue.

$$\omega_i = \frac{1}{\Delta t} \ln(\lambda_i) \tag{4}$$

A series of DMD analyses are carried out using a sliding time window. More details on the steps involved in DMD are provided in Appendix A.

The region of investigation for DMD is restricted to the vicinity of the laminar separation bubble as shown by the dashed lines in Fig. 4, in a reference frame fixed to the pitching airfoil. If a larger area encompassing the dynamic stall vortex (DSV) is included, the dynamics of the vortex masks the growth of instabilities around the separation bubble, which is our primary focus. The sampling time between snapshots should be such that the Nyquist sampling theorem is satisfied. As this requires an estimate of time scales inherent in the flow, WT was used to analyze C_p time series at different points on the wall near the LSB. WT provided a lower bound on the sampling time required to capture significant (i.e. having relatively high energy content) high-frequency components. The upper bound (i.e. total duration

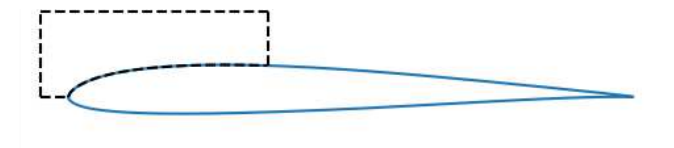


Fig. 4 Spatial domain used for DMD analysis

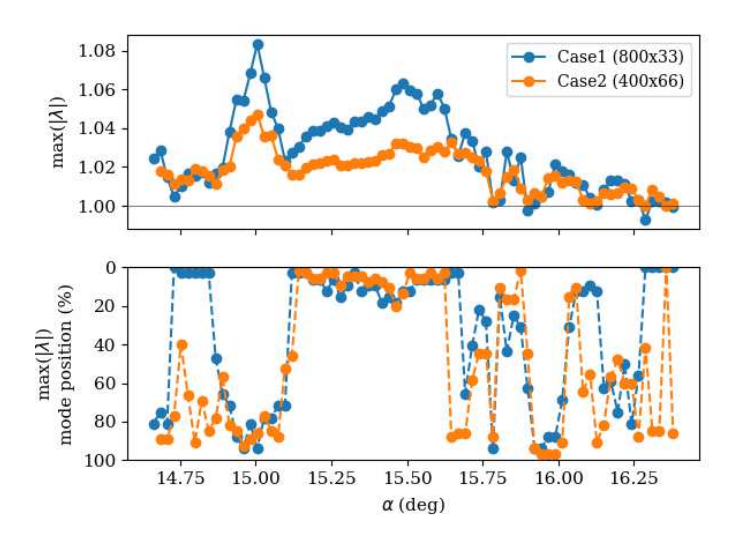


Fig. 5 SD7003 airfoil at Re_c 200,000, Top: Maximum eigenvalues with increasing α ; Bottom: Corresponding mode position in percent, with 0 being the most dominant, and 100, the least.

over which snapshots were taken) was estimated based on scale-averaged spectra. Details on WT are provided in section III.D.

Table 2 Time/frame spacing for DMD

	Δt /frames between snapshots	Total time/frames
Case 1	0.016 / 800	0.528 / 33
Case 2	0.008 / 400	0.528 / 66

The first row of Table 2 gives the relevant non-dimensional time scales $(t^* = U_{\infty}t/c)$ used to carry out DMD. A second set of analyses, corresponding to row 2 in Table 2, was carried out with twice the sampling rate of the first. A general observation in applying DMD to this flow field is that it was not amenable to order reduction, that is, representing the solution with a smaller set of eigenmodes (see Appendix A for details). Further, with the exception of a 'mean' flow mode, all other eigenmodes are found to be noisy, without the presence of any identifiable coherent structures.

Fig. 5 presents results from a set of consecutive DMD analyses shifted in time for the SD7003 airfoil at Re_c 200,000. Each point is plotted at the time corresponding to the central snapshot included in the analysis. The top panel shows the maximum of the absolute value of the eigenvalues, $\max(|\lambda|)$ obtained from each DMD analysis. These represent the fastest growing DMD modes at their respective times. $|\lambda| > 1$ corresponds to unstable DMD modes. The bottom panel shows the mode positions corresponding to the eigenvalues in the top panel, the most dominant being 0% and least being 100%. The mode positions are determined by arranging the modes in decreasing order of the magnitude of their weights $|b_i|$. Both cases listed in Table 2 are plotted.

We see that there are unstable eigenvalues ($|\lambda| > 1$) beginning at the first available data point. They seem to slowly converge to stable values towards the end of the last time window. The modes corresponding to the unstable eigenvalues become dominant around $\alpha \sim 15.1^{\circ}$ and remain dominant over a range of about 0.6° . However, no conclusions can

be drawn based on certain unstable eigenmodes being dominant over a small time window. Since all of them evolve exponentially with time, they all eventually become dominant. At later times, the magnitude of the largest eigenvalue drops and appears to converge to unity as shown in Fig. 5. It should be noted that the maximum eigenvalue plotted at each α is found from DMD analysis applied to a time window that extends to either side. Therefore, the entire plot shifted forward or aft in α by about 0.75° would also be valid.

Fig. 6 shows the corresponding plot for the NACA0012 airfoil at Re_c 500,000. While unstable eigenvalues are present throughout, they do not seem to be converging to unity within the region investigated, as in the previous case. This might reflect the more gradual stall undergone by the NACA0012 airfoil at this Re_c . The unstable modes are also the most dominant ones over a larger time duration. Comparing results from all cases, we are unable to find consistent trends across them. Further, the presence of unstable eigenvalues throughout the identified stall onset regime means that there is no distinguishing point that can be used as a marker for stall onset. In summary, while DMD has been effective in identifying large scale coherent structures (such as the DSV in pitching airfoils[11] and shed vortices in oscillating cylinders[18]), we find that its application to delineate instabilities around the laminar separation bubble region is unsuccessful.

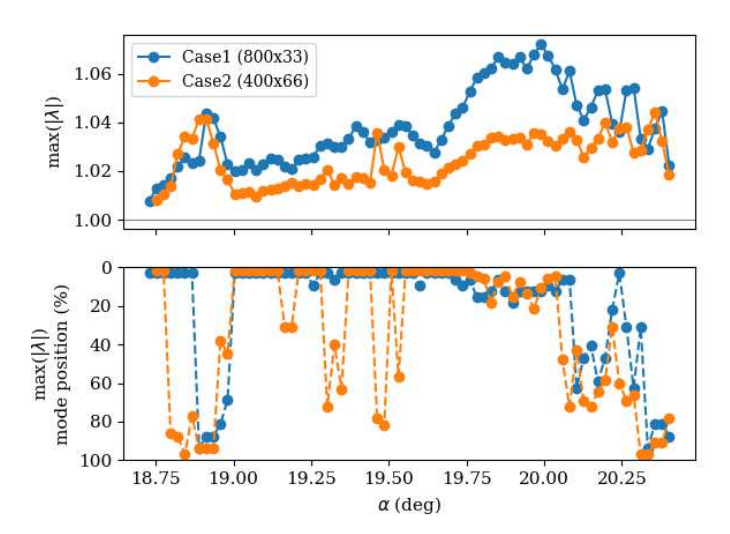


Fig. 6 Maximum eigenvalues (top) and corresponding mode positions (bottom) for the NACA0012 airfoil at Re_c 500,000.

D. Wavelet Transform

The Wavelet Transform (WT) is used to perform spectral analysis of non-stationary signals, by taking their cross-correlation with a wavelet function, a wave-like function which is localized in time and has a compact spectrum[19]. The wavelet function used is either continuous or discrete; our work uses the Continuous Wavelet Transform. While the short-time Fourier transform uses a fixed window length shifted in time to generate time-varying spectra, WT uses varying window lengths (or scales of the wavelet function) shifted in time to generate spectra that are a function of time as well as scale (frequency). One of the reasons for preferring the latter is its multi-resolution capability, which is required to resolve turbulent instabilities. Our goal in using WT was to find inherent time scales in the flow and their variation with time. Suppose we have a time series x(t). Its wavelet transform is defined by its cross-correlation with a wavelet function ψ , as given by Eq. (5).

$$T(a,b) = w(a) \int x(t)\psi^* \left(\frac{t-b}{a}\right) dt$$
 (5)

a is a measure of the length or scale of the wavelet along the time axis, while b represents its translation in time. This is schematically shown in Fig. 7. w(a) represents a weight used to scale the wavelet function of a given scale to have unit energy. We have chosen to use the complex Morlet wavelet for our analysis (see Appendix B for details). The contours of |T(a,b)| with respect to time and frequency, called the scalogram, is used to identify frequencies present at

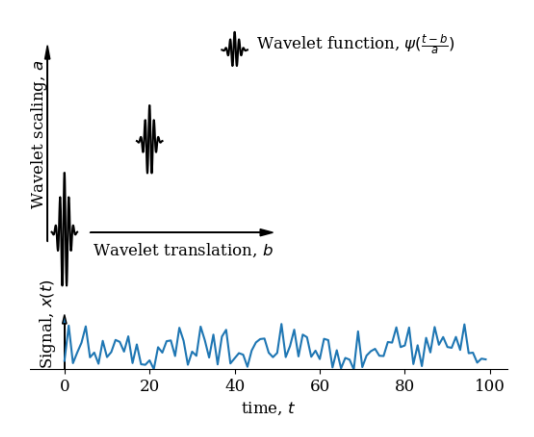


Fig. 7 Schematic of Wavelet Transform.

different times around the stall onset regime. We use time series of the pressure coefficient C_p at a point on the airfoil near the leading edge for performing WT. Since we are interested in the dynamics of the LSB, we consider C_p time series in its vicinity to be representative of the same. C_p time series at different points on the SD7003 airfoil at Re_c 500,000 are shown in Fig. 8.

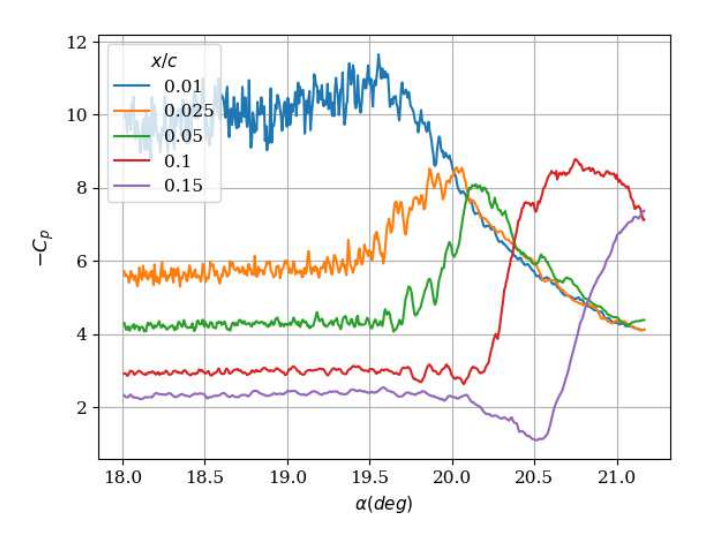


Fig. 8 C_p vs α at different points on the airfoil suction surface for SD7003, Re_c 500,000.

The magnitude (|T(a,b)|) and real part (Re[T(a,b)]) of the scalogram for this case are shown in Fig. 9. (Wavelet transforms have been performed using the Python package PyCWT[20].) The x-axis represents increasing α , while the y-axis represents $\log_2(a)$ plotted in reverse (small scales or high frequencies at the top, large scales or low frequencies at the bottom). The hatching on the plot indicates regions affected by the edge of the time series. Scales smaller than 2^{-5} are seen to be of universal nature for all times (see Fig. 9). A more conservative estimate is an upper bound of 2^{-6} . Thus, wavelet transforms provide an upper bound for the frequencies to be considered. The arrow in Fig. 9a indicates the generation of progressively more energetic smaller scales (increasing magnitude of T(a,b)) at moderate values of scale a). This is consistent with the general idea of an instability. The real part of T(a,b) shows the generation of coherent sinusoids at scales between 2^{-5} to 2^{-3} at larger α values. The large scale features greater than 2^{-2} are an artifact of edge effects. The observed energetic small scales can be explained by the increase in the variance of the signal after $\alpha = 19.6$, when the local average is discarded. Fig. 10 demonstrates the same.

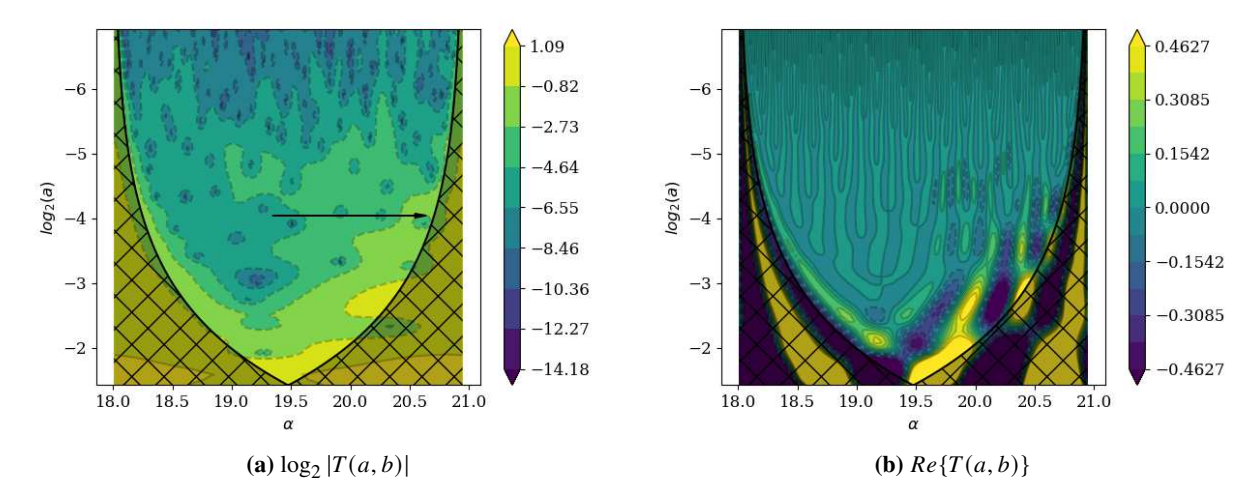


Fig. 9 Absolute value and real part of the wavelet transform function T(a, b) for SD7003 airfoil at Re_c 500,000.

The lower bound for frequency to be used in DMD was found using the power spectral density (PSD) obtained by averaging the square of the scalogram across time. This was done after detrending the signal (see Fig. 10) by decomposing it into intrinsic mode functions. Fig. 11 shows the PSD from WT along with PSD calculated from the Fourier transform of the signal. The dashed vertical line on the left indicates the smallest frequency that can be extracted using the Morlet wavelet. Based on the above analysis, the upper and lower bounds for frequencies were calculated as 60 Hz and 3 Hz respectively. The trends described above and timescales obtained remain the same for the C_p time series at another point in the vicinity of the LSB, namely, 0.15c. Hence, these values were used in the DMD analysis in section III.C.

The magnitude and real part of the scalogram are shown for the SD7003 airfoil at Re_c 200,000 in Fig. 12. These show the emergence of energetic small scales around 15.5°, which is towards the end of the stall onset regime (see Fig. 1). This is in contrast to the same airfoil at Re_c 500,000, where the structures appear well outside the stall onset regime (see Fig. 2)..

We also find that the scalogram obtained from WT is highly dependent on the spectra of the quantity chosen. The use of a different quantity whose statistics are distributed differently around stall onset (for example, the *BEF* which is noisier earlier in the stall onset regime), the observed energetic scales would correspondingly shift in time. Further, as already noted, energetic small scales are seen to exist within the stall onset regime in some cases and outside of it in others. This is clearly seen from Figs. 1 - 3 in section III.A.

IV. Conclusion

We have summarized our results from different approaches to characterize leading-edge dynamic stall onset in the present work. We first defined the stall onset regime as extending from the time of onset of instabilities within the LSB upto the formation of the DSV. Our goal was to find some distinguishing behavior within the stall onset regime from each of the three methods used, that would clearly indicate stall. The first method, namely, observing the time variation of two flow parameters (*LESP* and *BEF*), was effective in signaling the onset of stall, with the *BEF* reaching its critical value earlier than the *LESP*. The second, DMD, yielded unstable eigenvalues both within and outside the stall onset regime. The third, WT, showed the presence of energetic small scale structures, whose time of incidence varied relative to the stall onset regime for different cases with no observable trend. We did not find any distinguishing behavior from DMD or WT analysis that would clearly indicate stall onset, even though these two methods use information from different times in their calculation, in contrast to the flow parameters.

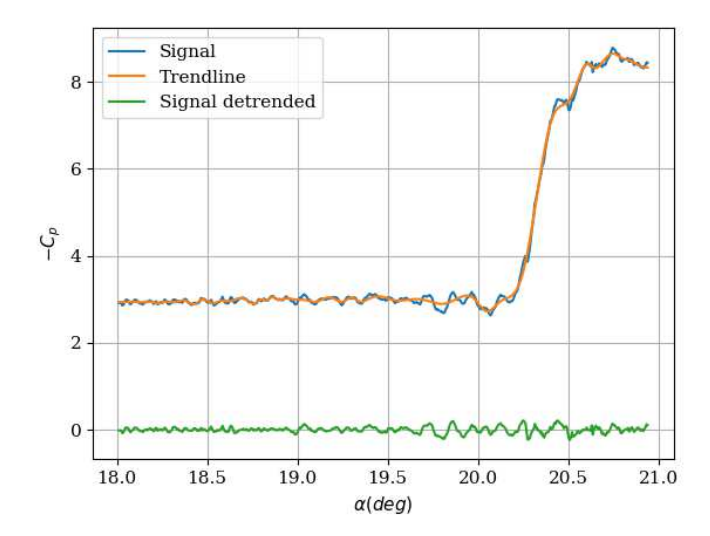


Fig. 10 C_p at x = 0.1c on the suction surface before and after detrending, for the SD7003 airfoil at Re_c 500,000.

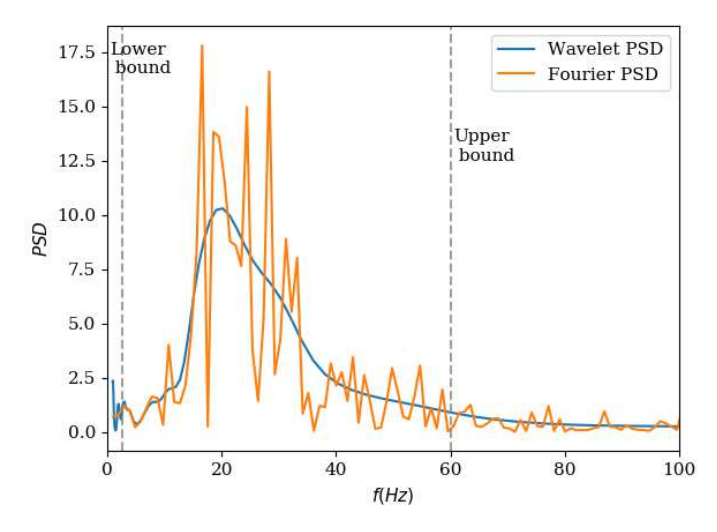


Fig. 11 Fourier and Wavelet PSD (found by averaging the scalogram across time after detrending) vs. frequency for SD7003 at Re_c 500,000.

Appendix

A. Dynamic Mode Decomposition

The DMD algorithm finds the best fit linear approximation for a sequence of flow states separated in time, or 'snapshots'. Typically, the velocity field is used to describe the flow field, although there is flexibility in choosing other flow variables of interest. By examining the time history of the largest eigenvalues obtained for a series of decompositions shifted in time, we can comment on the onset of instabilities. The steps involved in 'Exact DMD' [21, 22] are briefly summarized below.

The span-averaged, 2D velocity field in a reference frame fixed to the airfoil leading edge is arranged in columns as

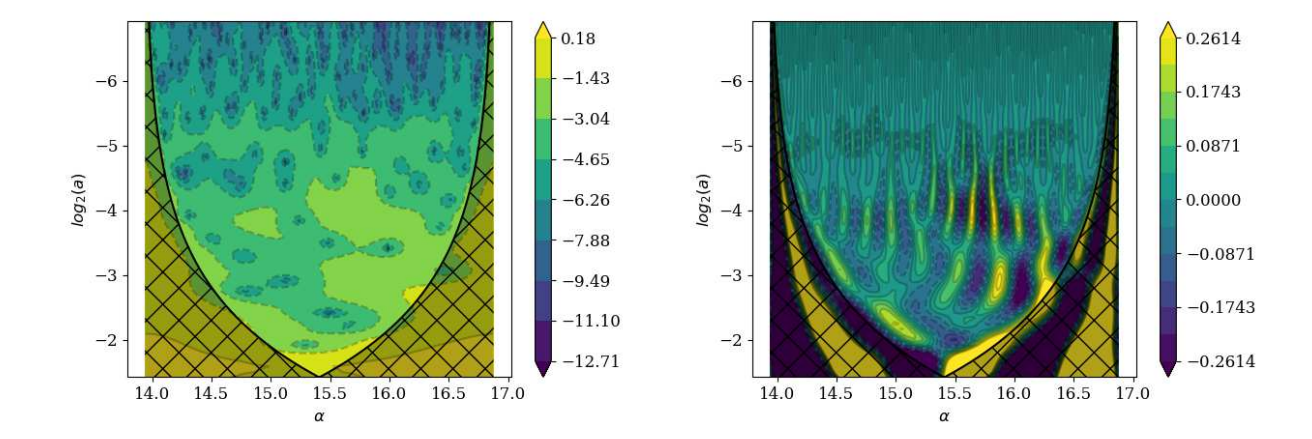


Fig. 12 Absolute value and real part of the wavelet transform function T(a, b) for the SD7003 airfoil at Re_c 200,000.

follows:

$$\begin{bmatrix} | & | & & | \\ x_1 & x_2 & . & . & . & x_m \\ | & | & & | \end{bmatrix}$$

where each column contains velocities u and v at all n grid points at a given time. Each column is separated by time Δt .

Writing columns $\mathbf{x_1}$ to $\mathbf{x_{m-1}}$ and $\mathbf{x_2}$ to $\mathbf{x_m}$ as matrices X_1 and X_2 respectively, we assume a linear transformation represented by matrix A exists between them. Hence, we can write:

$$X_2 \approx AX_1$$
 (6)

By carrying out an eigenvalue decomposition of \tilde{A} , an approximation to A, we obtain the solution at any time instant, $\mathbf{x}(t_k = k\Delta t)$ as a linear combination of the columns of Φ , the DMD modes, as shown in Eq. (7)..

$$\mathbf{x}(t_k) = \sum_{\substack{i=1,r\\r < -m-1}} \Phi_i \exp(\omega_i t_k) \mathbf{b_i}$$
 (7)

b is a vector of the weights multiplying each DMD mode, found from initial conditions at t = 0. Each DMD mode evolves at a specific frequency ω_i .

$$\omega_i = \frac{1}{\Lambda t} \ln(\lambda_i) \tag{8}$$

 λ_i is the i^{th} discrete-time eigenvalue. Each column of Φ corresponds to a given spatial mode. This is scaled by $\mathbf{b} \exp(\omega t)$ to obtain the flow field at any desired time. Φ has at most m-1 columns - if a dimensionality reduction is possible, this would be smaller. This process is repeated by shifting X_1 and X_2 in time and carrying out a series of DMD analyses to get a time history of maximum growth rate.

We observed that DMD applied to the current problem was not amenable to order reduction, that is, representing the solution with a smaller set of eigenmodes. This is indicated by the distribution of singular values of the snapshots under consideration, which is obtained from a singular value decomposition of matrix X_1 . The number of non-zero or non-negligible singular values, (say r, r <= m-1) determines the size of matrix \tilde{A} whose eigen-decomposition then gives the DMD modes. In our case, as shown in Fig. 13, it turns out that r = m-1, that is, none of the singular values

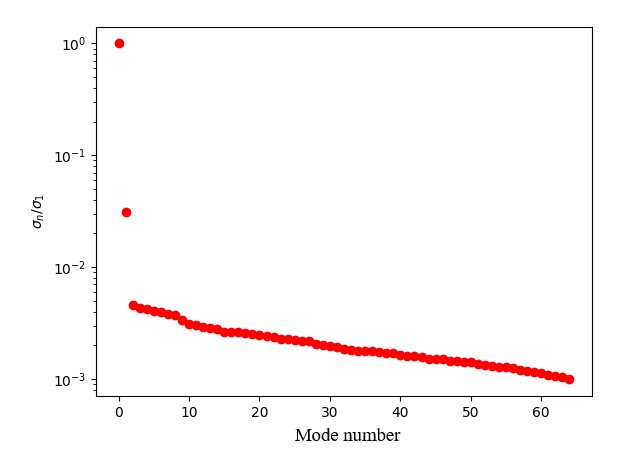


Fig. 13 Singular values of matrix X_1

can be neglected, because the largest and smallest values are separated only by an order of 10^{-3} . The x-axis in the figure corresponds to mode number (SVD, not DMD), and the y-axis, the singular values normalized by the maximum.

B. Wavelet Transforms

As defined in section III.D, the wavelet transform of a time series x(t) is obtained from its cross-correlation with a wavelet function ψ . The wavelet function is required to be compact in time and frequency and have zero mean Examples of suitable wavelet functions are the Morlet wavelet, derivatives of Gaussian (DOG) functions etc.

$$\psi(\eta) = \pi^{1/4} e^{i\omega_0 \eta} e^{-\eta^2/2} \tag{9}$$

In the present work, the complex Morlet wavelet defined by Eq. (9) is used. η is a non-dimensionalized time parameter and $\omega_0 = 6$ to satisfy the admissibility condition for a wavelet [23]. Compared to the Mexican hat and other DOG functions, the Morlet wavelet has higher resolution in the scale axis and is capable of resolving higher frequencies for a given sampling rate. Its features are more smeared out along the time axis and the lowest frequency it can resolve is about 2.7/t, where t is the total duration of the sample. However, the low frequency content excluded by the Morlet function is very close to the DC component. The scale of the wavelet is not necessarily the same as the Fourier period (inverse of Fourier frequency). However, they are close for the Morlet wavelet: the scale is 1.03 times the Fourier period.

It is recommended to remove the mean component of the signal [23], however, the mean is not clearly defined for a non-stationary time series. Comparing the wavelet transform of the original signal with and without detrending using a local average, we find that the trends observed from the scalogram do not depend on the low frequency components subtracted out from the original signal. This might be due to the lower bound on the frequency content that can be discerned using the Morlet wavelet. In order to remove the trend, we use Empirical Mode Decomposition to decompose the signal into Intrinsic Mode Functions. We then subtract one or more low frequency modes (considered to be the mean) from the signal and perform a wavelet analysis of the remainder.

Acknowledgements

Funding for this research is provided by the National Science Foundation (Grants CBET-1554196 and 1935255). Co-author Sharma acknowledges the support provided to him by the 2019 AFOSR Summer Faculty Fellowship. Computational resources are provided by NSF XSEDE (Grant #TG-CTS130004) and the Argonne Leadership Computing Facility, which is a DOE Office of Science User Facility supported under Contract DE-AC02-06CH11357. We acknowledge the assistance by Drs. Miguel Visbal and Daniel Garmann from the Air Force Research Laboratory in providing initial CFD solutions. We also acknowledge fruitful discussions with Prof. Paul Durbin on the topic.

References

- [1] Ramesh, K., Gopalarathnam, A., Granlund, K., Ol, M. V., and Edwards, J. R., "Discrete-vortex method with novel shedding criterion for unsteady aerofoil flows with intermittent leading-edge vortex shedding," *Journal of Fluid Mechanics*, Vol. 751, 2014, p. 500–538. https://doi.org/10.1017/jfm.2014.297.
- [2] Corke, T. C., and Thomas, F. O., "Dynamic Stall in Pitching Airfoils: Aerodynamic Damping and Compressibility Effects," Annual Review of Fluid Mechanics, Vol. 47, No. 1, 2015, pp. 479–505. https://doi.org/10.1146/annurev-fluid-010814-013632, URL http://www.annualreviews.org/doi/10.1146/annurev-fluid-010814-013632.
- [3] Doligalski, T., "Vortex Interactions with Walls," *Annual Review of Fluid Mechanics*, Vol. 26, No. 1, 1994, pp. 573–616. https://doi.org/10.1146/annurev.fluid.26.1.573.
- [4] Green, S., Fluid Vortices, Fluid Mechanics and Its Applications, Springer Netherlands, 2012.
- [5] Widmann, A., and Tropea, C., "Parameters influencing vortex growth and detachment on unsteady aerodynamic profiles," *Journal of Fluid Mechanics*, Vol. 773, 2015, pp. 432–459. https://doi.org/10.1017/jfm.2015.259.
- [6] McCroskey, W. J., "The phenomenon of dynamic stall," Tech. rep., NASA, Washington, DC, 1981.
- [7] Mulleners, K., and Raffel, M., "The onset of dynamic stall revisited," *Experiments in Fluids*, Vol. 52, No. 3, 2012, pp. 779–793. https://doi.org/10.1007/s00348-011-1118-y.
- [8] Chandrasekhara, M. S., "Compressible dynamic stall vorticity flux control using a dynamic camber airfoil," *Sadhana*, Vol. 32, 2007, pp. 93–102. https://doi.org/10.1007/s12046-007-0008-8.
- [9] Narsipur, S., Hosangadi, P., Gopalarathnam, A., and Edwards, J. R., "Variation of Leading-Edge Suction at Stall for Steady and Unsteady Airfoil Motions," *54th AIAA Aerospace Sciences Meeting*, 2016. https://doi.org/10.2514/6.2016-1354.
- [10] Sudharsan, S., Ganapathysubramanian, B., and Sharma, A., "A novel criterion to characterize leading-edge dynamic stall onset," , 2021. (under review).
- [11] Mariappan, S., Gardner, A. D., Richter, K., and Raffel, M., "Analysis of Dynamic Stall Using Dynamic Mode Decomposition Technique," AIAA Journal, Vol. 52, No. 11, 2014, pp. 2427–2439. https://doi.org/10.2514/1.J052858.
- [12] Peacock, T., and Haller, G., "Lagrangian coherent structures: The hidden skeleton of fluid flows," *Physics Today*, Vol. 66, No. 2, 2013, pp. 41–47. https://doi.org/10.1063/PT.3.1886.
- [13] Mulleners, K., and Raffel, M., "Dynamic stall development," Experiments in Fluids, Vol. 54, No. 2, 2013. https://doi.org/10.1007/s00348-013-1469-7.
- [14] Visbal, R. M., and Gaitonde, V. D., "On the Use of Higher-Order Finite-Difference Schemes on Curvilinear and Deforming Meshes," *Journal of Computational Physics*, Vol. 181, No. 1, 2002, pp. 155–185.
- [15] Sharma, A., and Visbal, M., "Numerical investigation of the effect of airfoil thickness on onset of dynamic stall," *Journal of Fluid Mechanics*, Vol. 870, 2019, p. 870–900. https://doi.org/10.1017/jfm.2019.235.
- [16] Wu, J.-Z., Ma, H.-Y., and Zhou, M.-D., Vortical Flows, Springer Berlin Heidelberg, 2015.
- [17] Schmid, P. J., "Dynamic mode decomposition of numerical and experimental data," *Journal of Fluid Mechanics*, Vol. 656, 2010, p. 5–28. https://doi.org/10.1017/S0022112010001217.
- [18] Jang, H. K., Ozdemir, C. E., Liang, J.-H. ., and Tyagi, M., "Oscillatory flow around a vertical wall-mounted cylinder: Dynamic mode decomposition," *Physics of Fluids*, Vol. 33, No. 2, 2021, p. 025113. https://doi.org/10.1063/5.0032644.
- [19] Addison, P., The Illustrated Wavelet Transform Handbook, Boca Raton: CRC Press, 2017. https://doi.org/https://doi.org.proxy.lib.iastate.edu/10.1201/9781315372556.
- [20] Krieger, S., Freij, N., Brazhe, A., Torrence, C., Compo, G. P., and contributors, 2017. https://pycwt.readthedocs.io/.
- [21] Tu, J. H., Rowley, C. W., Luchtenburg, D. M., Brunton, S. L., and Kutz, N., "On dynamic mode decomposition: Theory and applications," *Journal of Computational Dynamics*, Vol. 1, 2014, p. 391. https://doi.org/10.3934/jcd.2014.1.391.
- [22] Kutz, J. N., Brunton, S. L., Brunton, B. W., and Proctor, J. L., *Dynamic Mode Decomposition*, Society for Industrial and Applied Mathematics, Philadelphia, PA, 2016. https://doi.org/10.1137/1.9781611974508.
- [23] Torrence, C., and Compo, G. P., "A Practical Guide to Wavelet Analysis," *Bulletin of the American Meteorological Society*, Vol. 79, No. 1, 1998, pp. 61–78. https://doi.org/10.1175/1520-0477(1998)079<0061:APGTWA>2.0.CO;2.